



UNIVERSITEIT VAN AMSTERDAM

Subatomic Physics Workshop

Dr Juan Rojo

VU Amsterdam and Nikhef Theory Group

<http://www.juanrojo.com/>
j.rojo@vu.nl

Lecture notes, current version: January 11, 2017

Table of Contents

	Page
Course outline and schedule (theory lectures)	2
High-energy collisions	3
Electron-positron collisions	3
Lepton-proton collisions	5
Proton-proton collisions	9
The (Abelian) Higgs mechanism	15
Higgs production at the LHC	20
Jet reconstruction and substructure	24
Jet substructure	27

Course outline and schedule (theory lectures)

There will be **two theory sessions** for the Subatomic Physics Workshop:

- Monday 9th of January 2017
- Wednesday 11th of January 2017

The lectures will take place between **13.00** and **16.30**, with three one-hour slots divided by 15 min breaks, in **room H331**.

These theory lectures aim to provide a gentle introduction to high-energy particle collisions and to some important topics required for the interpretation of LHC physics. In detail, in these lectures we will cover:

- High-energy particle collisions
- Proton-proton collisions at the energy frontier: the Large Hadron Collider
- The Abelian Higgs mechanism
- Higgs production and decay at the LHC
- Jet reconstruction and substructure in hadronic collisions

Prior knowledge of special relativity, classical mechanics (the Lagrangian formalism) and electromagnetism (including the covariant description of Maxwell's equation) is assumed, but no other prior knowledge of high-energy physics is required.

These lectures notes are available online from

<http://juanrojo.com/teaching>

A list of additional reading material [1, 2, 3, 4, 5, 6, 7, 8, 9] is indicated in the bibliography.

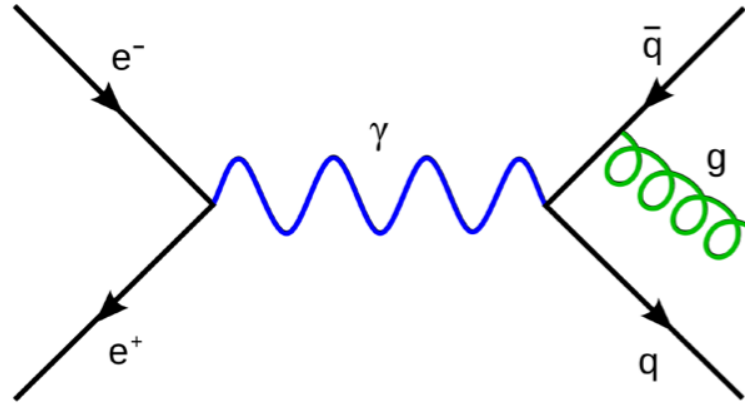


Figure 1: A collision between an electron and its anti-particle, the positron, which produces a virtual (intermediate) photon which then decays into a quark and antiquark pair, followed by the emission of a gluon from the latter.

High-energy collisions

First of all we review the different types of high-energy collisions between elementary particles that we can exploit to investigate the fundamental laws of nature at the smallest possible distances. These are first collisions between leptons (particles that do not experience the strong interaction, such as electrons or muons), then collisions between leptons and protons (or other hadrons, particles that are affected by the strong force) and finally proton-proton collisions such as those that take place at the LHC.

Electron-positron collisions

The simplest case of high-energy collisions are those involving leptons, fundamental particles that only interact via the electromagnetic and weak forces, but are not affected by the strong interaction. Collisions between electron and positrons were first realized in 1961 at the LNF in Frascati (Italy), with the ADA collider that able to achieve energies of up to 250 MeV. To date, the most powerful electron positron accelerator ever build is LEP, which operated at CERN in the 1990s, and that reached center-of-mass energies as large as 209 GeV. Further increases of the CoM of electron-positron colliders are very difficult due to synchrotron radiation, and a possibility that has been put forward is to build *linear* colliders such as ILC or CLIC.

In Fig. 1 we show the schematic representation of a collision between an electron and its anti-particle, the positron, which produces a virtual (intermediate) photon which then decays into a quark and antiquark pair, followed by the emission of a gluon from the latter. One of the main advantages of electron-positron colliders is that the energy of the collision is fixed and can be adjusted with high precision:

$$\sqrt{s} = (E_{e^+} + E_{e^-}) , \quad (1)$$

as opposed to *i.e.* LHC collisions where the energy of the *partonic collision* (that involving quarks and gluons) is unknown.

Electron-positron collisions have resulted in a number of fundamental discoveries in particle physics, such as the existence of the charm and bottom quarks. When diagrams of the form of Fig. 1 are computed, one finds that the propagation of the intermediate virtual particle (meaning *off-shell*, that is, $p^2 \neq m^2$) leads to

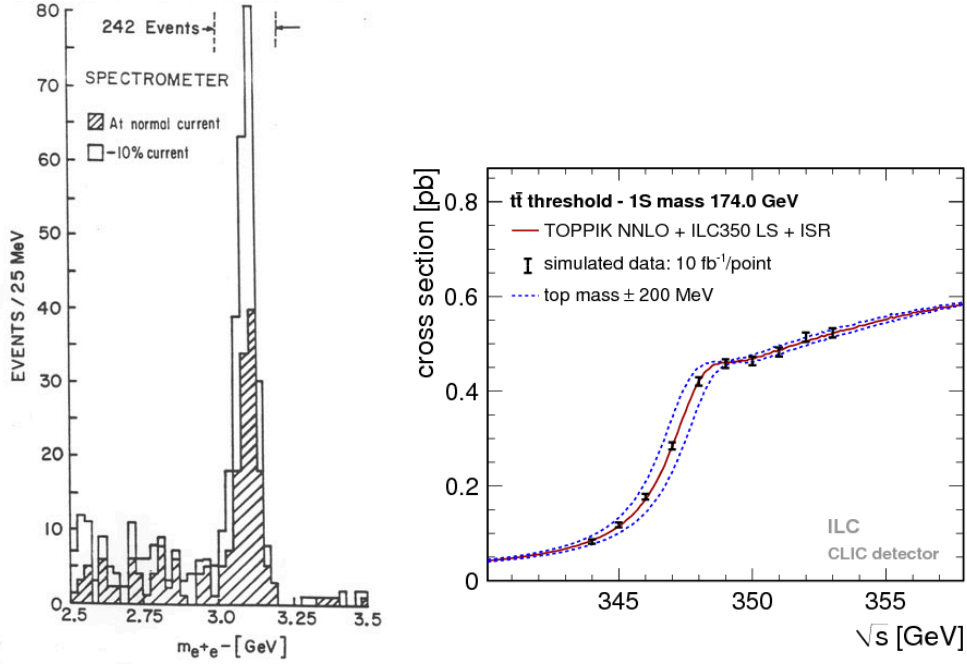


Figure 2: Left: the discovery of the charm quark in e^+e^- collisions: the existence of the so-called J/ψ particle (a bound state of charm and anticharm quarks) is seen from the peak in the collision energy $m_{e^+e^-}$ near the J/ψ mass ($\simeq 3.1$ GeV). Right: simulation of a scan near the top-antitop quark production threshold at $\sqrt{s} \simeq 350$ GeV which could be performed at a future high-energy e^+e^- collider [10].

a term in the scattering cross-section of the form

$$\sigma \sim \frac{1}{(s - m^2)^2 + m^2\Gamma^2}, \quad (2)$$

where m is the on-shell mass of intermediate particle, s is the center of mass energy Eq. (1) and Γ is the width of this particle (which determines how quickly it decays into other particles). From Eq. (2) we realize that the cross-section will be substantially *enhanced* when $\sqrt{s} \simeq m$. Therefore, a strong peak in the cross-section $\sigma(\sqrt{s})$ constitutes a clear direct evidence for the presence a new particle produced in the e^+e^- collision. In Fig. 2 we show the measurement that lead to the discovery of the charm quark in e^+e^- collisions: the existence of the so-called J/ψ particle (a bound state of charm and anticharm quarks) is seen from the peak in the collision energy $m_{e^+e^-}$ near the J/ψ mass ($\simeq 3.1$ GeV). On the right plot we show simulation of a scan near the top-antitop quark production threshold at $\sqrt{s} \simeq 350$ GeV which could be performed at a future high-energy e^+e^- collider. These peaks in invariant mass distributions of final-state particles, such as the one shown in Fig. 2, are one of the traditional ways to identify new particles for the first time.

Another important related discovery at electron-positron colliders was that of the evidence of a new quantum number, *color*, which is the analogous of the electric charge for the strong interactions. This information was provided by the measurement of the ratio of $\sigma(e^+e^- \rightarrow \text{hadrons})$ over $\sigma(e^+e^- \rightarrow \mu^+\mu^-)$, know as the R -ratio, defined as:

$$R(\sqrt{s}) \equiv \frac{\sigma(e^+e^- \rightarrow \text{hadrons})}{\sigma(e^+e^- \rightarrow \mu^+\mu^-)} = N_c \sum_{f=1}^{n_f} Q_f^2 \quad (3)$$

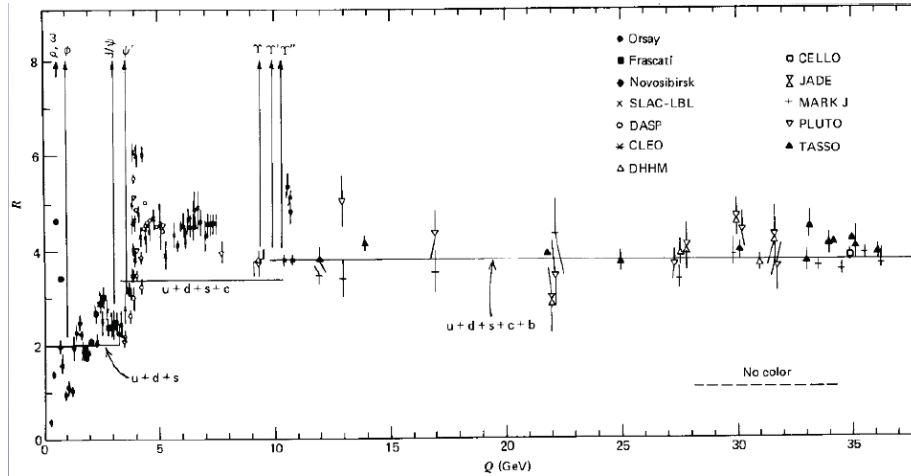


Figure 3: The ratio of hadron production in electron-positron annihilation over muon-antimuon pair, as a function of \sqrt{s} , the center-of-mass energy of the collision, for different experiments.

where the right-hand side of Eq. (3) follows from assuming the existence of n_f quarks, each one with electric charge Q_f . Crucially, the N_c pre-factor appears because each quark-antiquark can be produced in $N_c = 3$ different color states. In Fig. 3 we show the R ratio as a function of \sqrt{s} . The value of R depends on \sqrt{s} because only quarks that are characterized by $\sqrt{s} \geq 2m_q$ can be kinematically produced. Above the bottom threshold, $\sqrt{s} \geq 2m_b \simeq 10$ GeV, the value of the R -ratio stabilizes to

$$R_5 = \frac{11}{3} = 3 \left[2 \left(\frac{2}{3} \right)^2 + 3 \left(\frac{1}{3} \right)^2 \right], \quad (4)$$

As can be seen from Fig. 3, the data strongly disagrees with the possibility that quarks carry no color quantum number.

Lepton-proton collisions

Now we move to another class of high-energy particle collisions, those involving leptons (electrons, muons or neutrinos) with protons (or other hadrons, such as neutrons or deuterons). High-energy lepton-hadron collisions are known as the *deep-inelastic scattering* (DIS) processes. The main difference as compared to e^+e^- collisions is that protons are *not fundamental particles* but rather have internal structure in terms of their components, *quarks and gluons*, generically known as *partons*. This implies that, as we know show, the energy of the lepton-hadron collision is different from the energies of the *partonic collision* (involving quarks and gluons interacting with the incoming lepton).

The lepton-hadron collision proceeds via the exchange of a photon or a weak gauge boson (W or Z) between the lepton and the hadron, in a way that the (virtual) electroweak boson scatters off one of the quarks in the proton, as illustrated in Fig. 4. It is clear from Fig. 4 that the calculation of the cross-section of this process requires some knowledge of the likelihood of finding a quark or gluon in the proton with a given fraction x of its total proton momentum. Note that while E_p , the energy of the proton beam, is determined from the experimental set-up, the value of the *quark energy*, namely $E_q \simeq xE_p$, is in general different in each collision. The probability of finding a quark or gluon in the proton with a momentum fraction x is

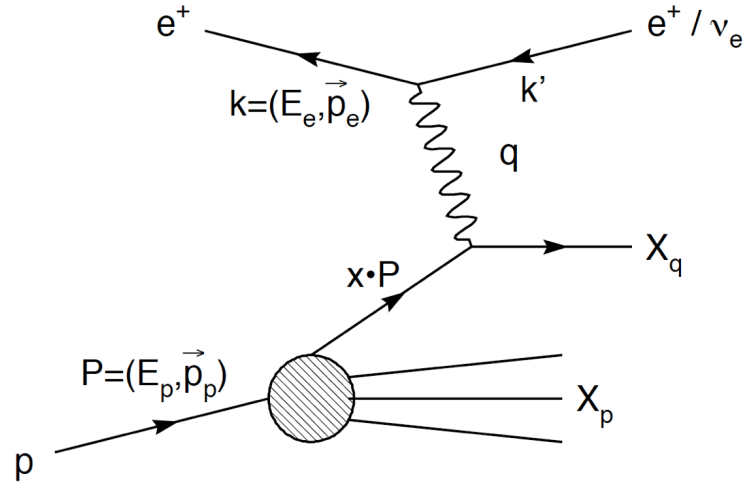


Figure 4: The deep-inelastic scattering process: the high-energy collision between a lepton, in this case a positron e^+ , and a proton p . The hard scattering takes place between an electroweak boson, in this case a photon, and a quark from the proton carrying energy $E_q = xE_p$ where E_p is the proton energy.

determined by *non-perturbative QCD dynamics*, and is given by the so-called *parton distribution functions* (PDFs), $q(x)$.

The kinematics of the deep-inelastic scattering process shown in Fig. 4 correspond to the following process:

$$e^-(k) + P(p) \rightarrow e^-(k') + X, \quad (5)$$

where p is the proton's momentum and k the lepton's momentum. In general the proton will be destroyed by the collision (hence the name *inelastic*). k' is the four-momentum of the scattered lepton, and X stands for the rest of the particles of the collision (including the proton remains). The actual values of p and k depend of the *reference frame* where the collision takes place:

- For *fixed-target* scattering, the proton is stationary (can be part of some gas or some solid target) and there is a lepton beam directed to this fixed target. In this case we have

$$p^\mu = (M_p, \vec{0}), \quad k^\mu = (k_z, 0, 0, k_z), \quad (6)$$

where we neglect the lepton mass and assume that the beam is directed in the z axis.

- For *collider* scattering instead, both the proton and the lepton are in motion and collide head-on with each other. In this case we find

$$p^\mu = (E_p, 0, 0, -p_z), \quad k^\mu = (k_z, 0, 0, k_z), \quad (7)$$

where the proton mass-shell condition implies $M_p^2 = E_p^2 - (p_z)^2$.

The main advantage of the collider kinematics is that the center-of-mass energy of the collision is substantially higher than in the fixed-target mode. For a fixed value of the lepton beam energy k_z , and assuming that

$k_z \gg M_p$, as corresponds to a high-energy collision, we have that in the fixed-target kinematics

$$p^\mu + k^\mu = (M_p + k_z, 0, 0, k_z), \quad \sqrt{s} = \sqrt{(p^\mu + k^\mu)^2} \simeq \sqrt{2M_p k_z}, \quad (8)$$

while for the collider kinematics instead one finds that

$$p^\mu + k^\mu = (E_p + k_z, 0, 0, k_z - p_z), \quad \sqrt{s} \simeq \sqrt{M_p^2 + 2k_z(E_p + p_z)} \simeq 2\sqrt{k_z E_p}, \quad (9)$$

and therefore larger by a factor $\sqrt{2E_p/M_p}$ (with $E_p \gg M_p$ in the high-energy regime) as compared to the fixed-target kinematics. Note that if $k_z = E_p$ (the lepton and proton beam have the same energies) then trivially the center of mass energy is $\sqrt{s} = 2E_p = 2k_z$.

The four-momentum transfer between the lepton and the proton (see Fig. 4) is given by

$$q \equiv k' - k, \quad (10)$$

where k' is the four-momentum of the outgoing lepton, which can be measured by the detector. Once we have measured k' , the kinematics of the deep-inelastic scattering process are then completely specified by the following variables

$$x_b \equiv \frac{Q^2}{2p \cdot q}, \quad Q^2 \equiv -q^2, \quad y \equiv \frac{q \cdot p}{k \cdot p}. \quad (11)$$

Here x_b is known as the *Bjorken* variable. Note from Eq. (11) that it is defined in terms of final-state momenta of the particles in the collision, and is, in principle, unrelated to the momentum fraction x carried by the PDFs in the proton. Moreover, since we are in the high-energy regime, we can take the approximation that $Q^2 \gg M_p^2$. For instance, the center-of-mass energy of the *proton-virtual photon collision* will be

$$W^2 \equiv (p + q)^2 = M_p^2 + Q^2 \frac{1 - x_b}{x_b} \simeq Q^2 \frac{1 - x_b}{x_b}. \quad (12)$$

The value $x_b = 1$ is known as the *elastic limit*, and corresponds to elastic collisions where the proton and the lepton scatter off each other without the former being destroyed.

Remarkably, it is possible under certain circumstances to identify x_b with the partonic x . To show this, we start by assuming that the quark carries a fraction x of the total momentum of the proton, that is, $\hat{p} \equiv x p$. Now recalling the definition of Bjorken- x , Eq. (11), which is a kinematical invariant, and applying momentum conservation (and neglecting the tiny light quark masses), we find that

$$\hat{p}' = \hat{p} + q, \quad (13)$$

$$(\hat{p}')^2 = 0 = (\hat{p} + q)^2, \quad (14)$$

$$Q^2 = 2\hat{p} \cdot q = 2x p \cdot q = Q^2 x / x_b, \quad (15)$$

and therefore we obtain that in the *parton model* the Bjorken- x_b variable, which is determined purely from the lepton kinematics, can be identified with x , the momentum fraction that the struck quark carries in the proton: $x_b = x$. So in DIS, to first approximation, we can directly access the momentum fraction carried by the quarks that constitute the proton.

Factoring out kinematic factors, the deep-inelastic scattering lepton-proton cross-section can be written in terms of a *structure function* $F_2(x_b, Q^2)$:

$$\frac{Q^4 x_b}{2\pi\alpha_{\text{QED}}^2 (1 + (1 - y)^2)} \frac{d^2\sigma^{\text{DIS}}}{dx_b dQ^2} = F_2(x_b, Q^2). \quad (16)$$

A key property of the structure function $F_2(x_b, Q^2)$ is that it can be directly measured from the kinematics of high-energy lepton-proton scattering using the variables defined in Eq. (11). In the *parton model* of the strong interactions (QCD), the structure function F_2 can be expressed as a convolution between the $\gamma^* q \rightarrow X$ hard-scattering partonic cross-section and the PDFs of the proton, which determine the likelihood of finding a quark or a gluon inside the proton carrying a fraction x of its momentum, as follows:

$$F_2(x_b) = x_b \sum_{q, \bar{q}} \int_{x_b}^1 \frac{dx}{x} f_q(x_b/x) \hat{\sigma}_{q\gamma^* \rightarrow X}(x), \quad (17)$$

where the sum runs over all the quarks and antiquarks in the proton that can couple to the virtual photon γ^* . Integrals of the form of Eq. (17) are often referred as *convolutions* between the PDFs and the matrix element, and represented by the symbol \otimes . At the first order in perturbation theory, the partonic cross-section is simply

$$\hat{\sigma}_{q\gamma^* \rightarrow X}(z) \sim e_q^2 \delta(z - 1), \quad (18)$$

and thus the structure function F_2 reads in this approximation

$$F_2(x_b) = x_b \sum_{q, \bar{q}} e_q^2 f_q(x_b), \quad (19)$$

and thus an experimental measurement of the DIS structure function provides direct information on the partonic structure of the proton.

The dependence of the PDFs with the momentum fraction x is a priori unknown, since it is determined by non-perturbative QCD dynamics. However, PDFs have still to satisfy a number of important sum rules, in particular the momentum sum rule,

$$\sum_{q, \bar{q}} \int_0^1 dx x f_q(x) = 1, \quad (20)$$

which translates the fact that the total momentum of the proton is distributed among all the quarks, and the valence sum rules

$$\int_0^1 dx (f_u(x) - f_{\bar{u}}) = 2, \quad (21)$$

$$\int_0^1 dx (f_d(x) - f_{\bar{d}}) = 1 \quad (22)$$

which ensure that the proton has the correct flavor quantum numbers (since one proton is composed by two valence up quarks and one valence down quark). These sum rules are also satisfied in perturbative QCD, and will be valid for all scales Q^2 : this is a direct consequence of the symmetries of the QCD Lagrangian. In the case of the momentum sum rule, it is necessary to include the contribution from the *gluon PDF* as well.

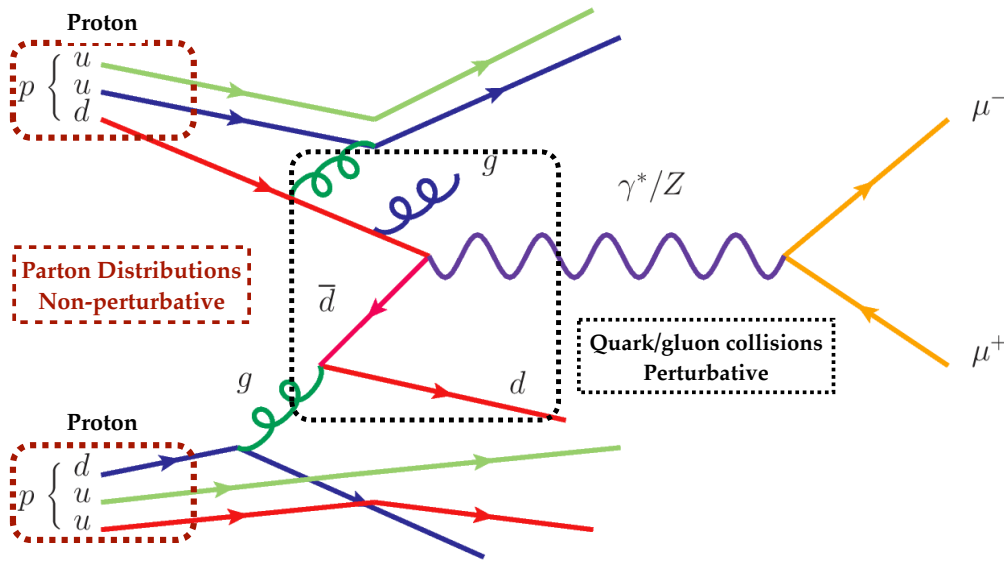


Figure 5: Representation of a proton-proton collision at the LHC, where two of the quarks or gluons that compose the protons undergo a energetic scattering, in this case leading to the production of a Z boson which then decays into a pair of muons. The cross-section for the scattering between quarks, gluons, and the Z boson can be computed in QCD perturbation theory, but the energy distributions of these same quarks and gluons inside the protons, the *parton distribution functions* (PDFs), are instead determined by non-perturbative QCD dynamics.

In the full theory of the strong interactions, this qualitative parton-model picture can be made quantitative by means of the *QCD factorization theorem*. In particular, in the presence of perturbative QCD corrections, the PDFs acquire a scale dependence $q(x, Q^2)$ with the hard-scattering scale of the process. In other words, the internal structure of the proton becomes dependent on the energy of the probe that we use to examine it, just as in microscopy the resolution that we can achieve depends on the wavelength of the probe.

Proton-proton collisions

Following the discussion of electron-positron and lepton-proton collisions, now we turn to discuss high-energy collisions between protons. In Fig. 5 we show the schematic representation of of a proton-proton collision at the LHC, where two of the quarks or gluons that compose the protons undergo a energetic scattering, in this case leading to the production of a Z boson which then decays into a pair of muons.

As in the case of lepton-proton collisions, also here the *matrix-element cross-section for the scattering between quarks, gluons, and the Z boson* can be computed in QCD perturbation theory, but the energy distributions of these same quarks and gluons inside the protons, the *parton distribution functions* (PDFs), are instead determined by non-perturbative QCD dynamics. Crucially, the *QCD factorization theorem* ensures that the same PDFs that appear in lepton-proton collisions are the ones suitable for the description of proton-proton scattering.

Schematically, the scattering cross-section for a proton-proton collision such as in the one in Fig 5 reads

$$\sigma_{\text{pp}}(\sqrt{s} = 2E_p) \simeq \sum_{f_1} \sum_{f_2} \tilde{\sigma}_{f_1 f_2}(E_{f_1}, E_{f_2}) \otimes q_{f_1}(x_{f_1}) \otimes q_{f_2}(x_{f_2}), \quad (23)$$

where we assume that the collision is symmetric (the two proton beams have the same energy, $\sqrt{s} = 2E_p$) and the sum runs over all possible quarks and gluons f_1 and f_2 that compose the two colliding protons respectively. As mentioned above, the \otimes symbol stands for a convolution integral between the PDFs and the partonic cross-section. In the case of a single dominant partonic channel, for instance gluon-gluon scattering, Eq. (23) simplifies to

$$\sigma_{pp}(\sqrt{s} = 2E_p) \simeq \tilde{\sigma}_{g_1 g_2}(E_{g_1}, E_{g_2}) \otimes g(x_1) \otimes g(x_2) . \quad (24)$$

Note that the partonic cross-section, giving the probability of the scattering between partons f_1 and f_2 , depends only on the partonic energies, $E_{f_1} = x_{f_1} E_p$ and $E_{f_2} = x_{f_2} E_p$, rather than on the proton's total energy. We also note that while the energy of the proton-proton collision $\sqrt{s} = 2E_p$, is known since it is fixed by the beam energy, in general the energy of the *partonic* collision between quarks and gluons is unknown. Adding the four-momenta of the two colliding partons, we find

$$p_1 + p_2 = E_p (x_1 + x_2, 0, 0, x_1 - x_2) , \quad (25)$$

and the total energy of the partonic collision is thus

$$\sqrt{\hat{s}} = 2E_p \sqrt{x_1 x_2} , \quad (26)$$

and thus depends on the probability distribution for x_1 and x_2 provided by the non-perturbative PDFs. This implies that in general, the hadronic center of mass frame energy \sqrt{s} will be different to the partonic center of mass frame energy $\sqrt{\hat{s}}$, and these two frames will only coincide when the colliding partons carry the same momentum fraction, $x_1 = x_2$.

An important consequence of this discussion is that in hadronic collisions the most suitable event description is provided by quantities that are either *invariant* or that *transform in a simple way* under *longitudinal boosts*, to decrease the sensitivity to this unknown initial state longitudinal momentum). Note that in an hadron-hadron collision is in general difficult to measure the total energy involved, due to detector limitations (incomplete angular coverage).

Let us therefore discuss which are the kinematic variables which are more adequate to describe hadron-hadron collisions. An important difference as compared to e^+e^- annihilation is that in hadronic collisions, the total longitudinal momentum of the partonic collision is unknown (determined by the PDFs) and it varies event by event. A suitable parameterization for four-momenta in hadronic collisions is can be constructed as follows. We begin by expressing the four-momentum p^μ of a final-state particle in polar (spherical) coordinates:

$$p = (E, p_x, p_y, p_z) = \left(\sqrt{\vec{p}^2 + m^2}, |\vec{p}| \sin \theta \cos \phi, |\vec{p}| \sin \theta \sin \phi, |\vec{p}| \cos \theta \right) \quad (27)$$

where θ is the polar angle with respect to the hadron beam, ϕ is the azimuthal angle with respect also to the hadron beam axis, as shown in Fig. 6, and the rest mass of the particle is denoted by m . This parametrization respects of course the mass-shell condition, $p^2 = m^2$.

Now, it is useful to express the four-momentum p in terms of two variables called respectively the particle's *rapidity* y and *transverse mass* m_T , defined as,

$$y \equiv \frac{1}{2} \ln \frac{E + p_z}{E - p_z}, \quad m_T \equiv \sqrt{p_T^2 + m^2}, \quad (28)$$

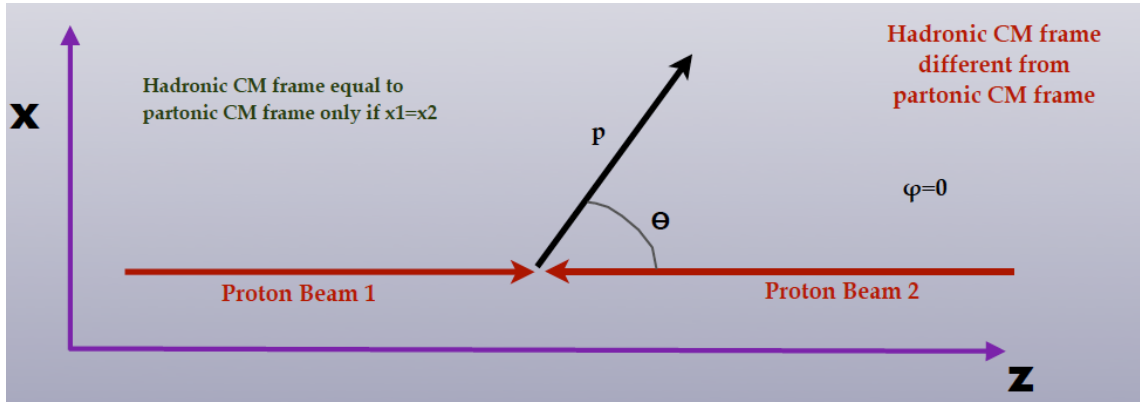


Figure 6: Kinematics of an hadron-hadron collision for an azimuthal angle of $\phi = 0$. In general, the hadronic center of mass frame will be different to the partonic center of mass frame.

and in terms of these two variables the parametrisation Eq. (27) can be written as follows

$$p = (E, p_x, p_y, p_z) = (m_T \cosh y, |p_T| \cos \phi, |p_T| \sin \phi, m_T \sinh y) . \quad (29)$$

In Eq. (29), the transverse mass and the particle transverse momentum's p_T are obviously invariant under longitudinal boosts, while the rapidity transforms additively, facilitating the transformation from the partonic center-of-mass the hadronic center-of-mass. To derive Eq. (29) from Eq. (27), note that

$$\cosh y = \frac{1}{2} \left(\left(\frac{E + p_z}{E - p_z} \right)^{1/2} + \left(\frac{E - p_z}{E + p_z} \right)^{1/2} \right) = \frac{E}{\sqrt{m^2 + p_T^2}} = \frac{E}{m_T} \quad (30)$$

and likewise for the other component of the four-momentum: it is only a change of variables, so the two parametrization are interchangeable.

It is easy to show that the rapidity y transforms *additively* under longitudinal boosts. Recall that under a longitudinal boost (that is, a boost in the z (beam) direction), a four-momentum transforms as

$$p \rightarrow p' = \gamma (E - \beta p_z, p_x, p_y, -\beta E + p_z) , \quad (31)$$

in terms of the usual Lorentz boost parameters

$$\beta = v, \quad \gamma = \frac{1}{\sqrt{1 - v^2}} , \quad (32)$$

so one can check that the rapidity transforms as

$$y \rightarrow y' = y + \frac{1}{2} \log \frac{1 - \beta}{1 + \beta} , \quad (33)$$

which has the important consequence that the difference between rapidities is boost invariant:

$$\Delta y' \equiv y'_1 - y'_2 = \Delta y \equiv y_1 - y_2 . \quad (34)$$

Another important variable for the description of hadron-hadron collisions is known as *pseudo-rapidity*.

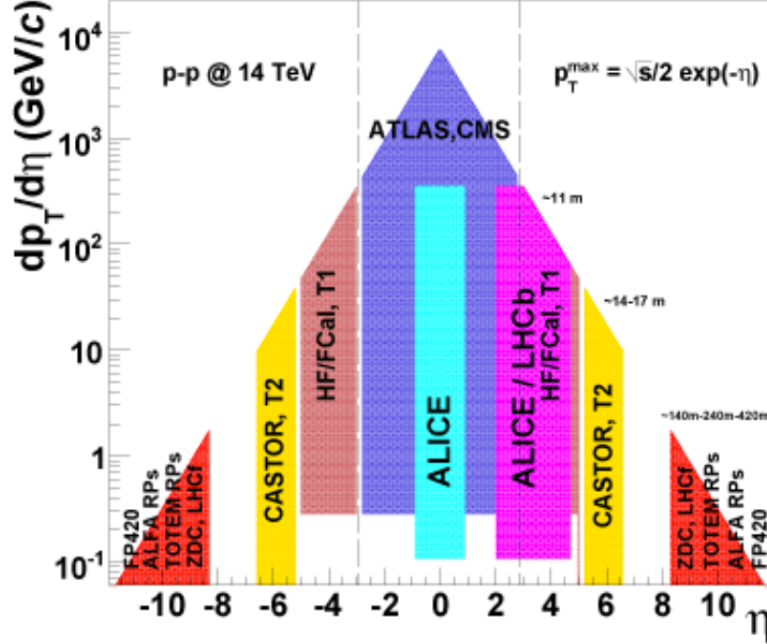


Figure 7: Approximate coverage in transverse momentum p_T and pseudo-rapidity η of current and future LHC detectors. For a given \sqrt{s} and pseudo-rapidity η , the kinematically maximum available p_T is $p_T^{\max} \simeq \sqrt{s} e^{-\eta}/2$.

In the limit of massless particles (defined as the limit in which $m \ll p_T$), the rapidity can be approximated by this pseudo-rapidity,

$$y \simeq \eta \equiv -\log \tan \frac{\theta}{2}, \quad (35)$$

which is often used in experimental analyses since it can be directly related to the geometrical acceptance of the detector. To check this property, note that when $m \ll p_T$, then $m_T \simeq p_T$, and therefore the four-momentum of a massless particle becomes

$$p \simeq p_T (\cosh y, \cos \phi, \sin \phi, \sinh y), \quad (36)$$

or alternatively

$$p = E (1, \sin \theta \cos \phi, \sin \theta \sin \phi, \cos \theta), \quad (37)$$

and therefore we can write the rapidity as

$$y \simeq \frac{1}{2} \ln \frac{1 + \cos \theta}{1 - \cos \theta} = -\ln \tan \frac{\theta}{2} = \eta \quad (38)$$

where we have used $p_z \simeq E \cos \theta$ for massless particles.

The usefulness of the pseudo-rapidity η is that it directly relates with the *geometrical acceptance* of a given particle detector, and thus can be directly matched to experimental measurements. The rapidity y instead needs to be constructed from separate measurements of the total particle energy E and its longitudinal momentum p_z , and measuring energies might be more difficult than measuring directions). Achieving the maximum possible coverage in pseudo-rapidity is a very important feature of a detector for hadron colliders, since this way one can access processes in the forward region. In Fig. 7 we show the approximate coverage

in transverse momentum p_T and pseudo-rapidity η of current (and proposed) LHC detectors. The two main purpose detectors, ATLAS and CMS, can cover up to $\eta \sim 2.5$, extended to $\eta \sim 4$ with the forward calorimeters, while LHCb is a forward experiment with acceptance $2.0 \leq \eta \leq 4.5$. Other, smaller experiments like TOTEM increase the coverage of the forward region, and are important for a variety of analysis like the total pp cross-section or the validation of predictions for high-energy cosmic ray production.

For a given pseudo-rapidity η and hadronic center-of-mass energy \sqrt{s} , there will be a maximum value of the p_T that can be accessed in these collisions. Assuming that the proton-proton collisions produces only two massless particles, by energy conservation in the laboratory frame their four momenta will be

$$p_1 \simeq p_T (\cosh \eta, \cos \phi, \sin \phi, \sinh \eta) , \quad (39)$$

$$p_2 \simeq p_T (\cosh \eta, -\cos \phi, -\sin \phi, -\sinh \eta) , \quad (40)$$

since the three-momenta \vec{p}_1 and \vec{p}_2 will be back-to-back. This means that

$$p_1 + p_2 = (2 \cosh \eta, \vec{0}) = (\sqrt{s}, \vec{0}) , \quad (41)$$

and thus we get the relation that

$$p_T^{\max} = \frac{\sqrt{s}}{2} \frac{1}{\cosh \eta} \simeq \frac{\sqrt{s}}{2} e^{-\eta} . \quad (42)$$

Therefore, the maximum *partonic center of mass energy* (indicated by the value of p_T) is achieved for central collisions, $\eta = 0$. This means that the central region is crucial for searches of new BSM massive particles, while the forward region is very important to keep full kinematical coverage for lighter states around the electroweak scale, including the production of Higgs bosons.

Moreover, LHC measurements in the forward region provide important information for high-energy astrophysics experiments such as cosmic ray detection or neutrino telescopes, since they correspond to a similar kinematical coverage when boosted from the center of frame (for the LHC detectors) to the laboratory center of mass frame (for cosmic ray collisions).

The Drell-Yan process. One the most representative processes of high-energy proton-proton collisions is the production of *electroweak vector bosons*, the W and Z bosons. Their large mass ($m_W \simeq 80$ GeV and $m_Z \simeq 90$ GeV) implies that they can only be produced if the collision energy is high enough, though indirect effects of their presence can already be inferred from lower energy experiments (such as nuclear β decays). The production of weak gauge bosons in hadronic collisions is of importance for a number of reasons, such as precision tests of the Standard Model, background to many searches for New Physics as well as input to global analysis of the proton structure by means of measurements of the Parton Distribution Functions.

In electroweak theory, at leading order the total *partonic cross-section* for the production of a weak gauge boson turns out to be schematically

$$\hat{\sigma} = \frac{4\pi^2}{3} \frac{g^2}{4\pi} \delta(\hat{s} - M_V^2) , \quad (43)$$

that is, the production cross-section is only non-zero where the partonic center of mass energy coincides with the mass of this specific gauge boson.

Following our previous discussion of the QCD parton model, Eq. (17), to compute the *hadronic cross-*

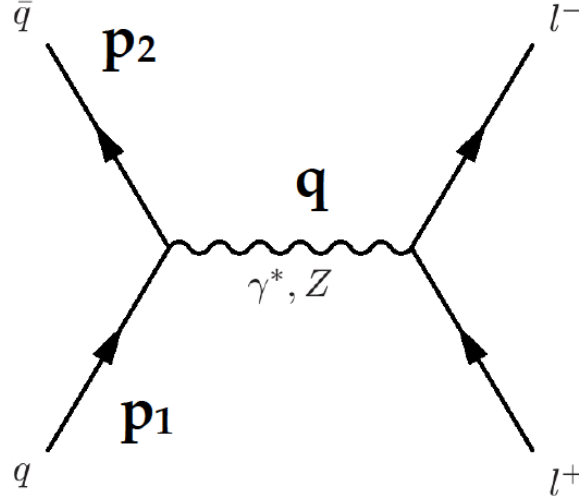


Figure 8: Feynman diagram for the hadroproduction of a neutral gauge boson, followed by the decay into two leptons, in the Born approximation. The four-momenta of the incoming quarks are labeled as p_1 and p_2 .

section we need to convolute the partonic cross-section Eq. (43) with the PDFs of the proton for those combinations of quark and gluons that can produce an electroweak boson (keeping into account quantum number conservation). For instance, in the specific case of W^+ production, in the parton model, and keeping only the contribution from the first two generations of quarks and anti-quarks for simplicity, assuming a *diagonal CKM mixing matrix*, we obtain for the hadronic cross-section

$$\sigma_{W^+} = \int dx_1 dx_2 [f_u(x_1)f_{\bar{d}}(x_2) + f_{\bar{d}}(x_1)f_u(x_2)] \times \frac{\pi^2}{3} \frac{\alpha_{\text{QED}}}{\sin^2 \theta_W} \delta(sx_1x_2 - M_W^2), \quad (44)$$

since only the scattering between a u quark and a \bar{d} quark has the correct quantum numbers to produce a W^+ boson. Performing the integral over the Dirac delta function in Eq. (44) we thus find

$$\sigma_{W^+} = \frac{\pi^2}{3} \frac{\alpha_{\text{QED}}}{\sin^2 \theta_W} \frac{1}{s} \int dx_1 \frac{1}{x_1} [f_u(x_1)f_{\bar{d}}(M_W^2/x_1s) + f_{\bar{d}}(x_1)f_u(M_W^2/x_1s)] , \quad (45)$$

that is, an integral over the proton PDFs determines the total production cross-section. Of course not all the values of x_1 are allowed in the integral Eq. (45) since there are some restrictions imposed by kinematical constraints. In particular, the requirement that $x_{1,2} \geq 1$ implies that the lower limit of the integral is $x_1^{\text{min}} = M_W^2/s$. In other words, the smaller that hadronic center-of-mass energy \sqrt{s} the smaller the value of x_1^{min} that will be relevant for W boson production. At the LHC with $\sqrt{s} = 13$ TeV, we find that $x_1^{\text{min}} = 4 \cdot 10^{-5}$ (though this assumes a detector with perfect coverage in rapidity).

Let us take a closer look at the kinematics of the Drell-Yan process. As indicated schematically in Fig. 8, the four-momenta of the two colliding partons can be parametrized as

$$p_1 = (x_1\sqrt{s}/2, 0, 0, x_1\sqrt{s}/2) , \quad (46)$$

$$p_2 = (x_2\sqrt{s}/2, 0, 0, -x_2\sqrt{s}/2) \quad (47)$$

$$q = ((x_1 + x_2)\sqrt{s}/2, 0, 0, (x_1 - x_2)\sqrt{s}/2) , \quad (48)$$

with q then being the four-momentum of the intermediate gauge boson. In this process, the kinematics are uniquely fixed once the gauge boson rapidity is specified. Indeed, it is easy to check, using the definition of y , that

$$y = \frac{1}{2} \log \frac{q_0 + q_z}{q_0 - q_z} = \frac{1}{2} \log \frac{x_1}{x_2}, \quad (49)$$

$$x_1 x_2 s = M_W^2, \quad (50)$$

and no other variables are required to describe the final state kinematics, since this is a $2 \rightarrow 1$ process. To derive Eq. (50), we have used the on-shell condition, namely, that $q^2 = M_W^2$ (note that we can do this only when working at the Born level). Therefore the values of the PDF Bjorken- x probed in this process are fixed once the vector-boson rapidity is specified, and are given by

$$x_1 = \frac{M_W}{\sqrt{s}} e^y, \quad x_2 = \frac{M_W}{\sqrt{s}} e^{-y}, \quad (51)$$

so one parton will carry a larger momentum fraction than the other. For partons produced at central rapidity, $y = 0$ and $x_1 = x_2 = M_W/\sqrt{s}$. Using Eq. (51) it is possible to determine the coverage in (x_1, x_2) that a given collider has access to. For instance, at the LHC 14 TeV, for ATLAS and CMS, that have $y \leq 2.5$, we find that $x_1(x_2) = 0.07(5 \cdot 10^{-4})$, while for the LHCb detector, whose acceptance goes up to $y \leq 4.5$, we find instead $x_1(x_2) = 0.5(6 \cdot 10^{-5})$. We see that forward measurements have an increased sensitivity to the small- x region of the proton structure.

Note that at the Born level, that is, when the only contribution to the production of a W boson is given by the diagram of Fig. 8, the W boson is produced without any transverse momentum ($p_T = 0$) and thus it would not be possible to detect since it would escape through the beam pipe. The p_T of W bosons, that makes its detection possible, can be generated by QCD perturbative radiative corrections as well as by soft non-perturbative QCD dynamics. Note also that in general all possible quark and antiquark combinations will contribute to the production cross-section, so in Eq. (45) one needs to include as well terms as $c\bar{s}$ (which is Cabibbo-enhanced) and $u\bar{s}$ (which is instead Cabibbo-suppressed).

The (Abelian) Higgs mechanism

Following this brief introduction to high-energy particle collisions, we turn to discuss a more formal topic which is however central for modern particle physics, namely *electroweak symmetry breaking*.

In the Standard Model of particle physics, the Higgs mechanism is responsible for giving mass to the W and Z bosons without *explicitly breaking* the gauge invariance of the theory, which would make them internally inconsistent. Here we present a simpler version of the Higgs mechanism, the *abelian case*, which illustrates how it would be possible to give *mass to the photon* while preserving gauge invariance of electromagnetism. This is the so-called *Abelian Higgs mechanism*.

Let us start with the classical *Lagrangian* of electromagnetism. In the *covariant formulation* of electromagnetism, the basic object is the electromagnetic *field-strength tensor*, defined as

$$F_{\mu\nu} = \partial_\mu A_\nu - \partial_\nu A_\mu, \quad (52)$$

where A_μ is the four-vector potential. In terms of $F_{\mu\nu}$, the Lagrangian density for electromagnetism reads

$$\mathcal{L} = -\frac{1}{4}F_{\mu\nu}F^{\mu\nu}, \quad (53)$$

where we assume that there are no free charges (in other words, we set to zero the four-current $j^\mu = 0$). From this Lagrangian, Maxwell's equations in the covariant formalism can be derived from a *variational principle*, in particular using the Euler-Lagrange equation

$$\partial_\mu \left[\frac{\partial \mathcal{L}}{\partial (\partial_\mu A_\nu)} \right] - \frac{\partial \mathcal{L}}{\partial A_\nu} = 0, \quad (54)$$

which leads to the equations of motion of the electromagnetic field in vacuum

$$\partial_\mu F^{\mu\nu} = 0, \quad \partial_\mu \tilde{F}^{\mu\nu} = 0. \quad (55)$$

To see this, note that if we expand the Lagrangian Eq. (53) in terms of the vector potential A_μ we find, up to overall constants,

$$\mathcal{L} \sim (\partial_\mu A_\nu \partial^\mu A^\nu - \partial_\mu A_\nu \partial^\nu A^\mu - \partial_\nu A_\mu \partial^\mu A^\nu + \partial_\nu A_\mu \partial^\nu A^\mu), \quad (56)$$

and if now we apply the Euler-Lagrange equation Eq. (54) we find, among other constraints, that

$$\left[\frac{\partial \mathcal{L}}{\partial (\partial_\mu A_\nu)} \right] \sim (\partial^\mu A^\nu - \partial^\nu A^\mu) \sim F^{\mu\nu}, \quad (57)$$

from which Maxwell's equations in vacuum follow, Eq. (55). It is possible to derive the three other Maxwell's equations in terms of $vecE$ and \vec{B} in a similar way.

From the covariant expression of Maxwell's equations, Eq. (55), the standard Maxwell's equation can be recovered replacing $A^\mu = (\phi, \vec{A})$ in terms of its components in a specific reference frame, where $\vec{E} = -\nabla\phi$ and $\vec{B} = \nabla \times \vec{A}$ in terms of the electric and magnetic potentials respectively. For example, if we take the $\nu = 0$ component of $\partial_\mu F^{\mu\nu}$, we find

$$\partial_\mu F^{\mu,0} = \partial_t F^{00} + \partial_x F^{10} + \partial_y F^{20} + \partial_z F^{30} = +\partial_x E_x \partial_y E_y + \partial_z E_z = \nabla E = 0, \quad (58)$$

which is Gauss' law of electromagnetism in vacuum.

A basic property of the Lagrangian Eq. (53) is its invariance under *gauge transformation* of the vector potential for an specific symmetry group. In particular, it is possible to verify that the Lagrangian Eq. (53) (and also $F_{\mu\nu}$ as well) is invariant under a transformation of the form

$$A_\mu(x) \rightarrow A_\mu(x) + \partial_\mu \eta(x), \quad (59)$$

where $\eta(x)$ is an *arbitrary function* of the space-time coordinates x^μ . In the mathematical language of *group theory*, this corresponds to a $U(1)$ rotation of the fields of the theory, in other words, a rotation of along the length of a circle. To verify this property, we note that from its definition we have that the gauge

transformation Eq. (59) will change the field-strength tensor as follows

$$F_{\mu\nu} = \partial_\mu A_\nu - \partial_\nu A_\mu \rightarrow \partial_\mu (A_\nu + \partial_\nu \eta) - \partial_\nu (A_\mu + \partial_\mu \eta) = F_{\mu\nu}, \quad (60)$$

because the partial derivatives commute among them, $\partial_\mu \partial_\nu \eta = \partial_\nu \partial_\mu \eta$. Since the Lagrangian is invariant under this gauge transformation, also the equations of motion for the fields of the theory (Maxwell's equations) will be likewise unchanged. Note that the statement that our theory should be invariant under transformations of the form Eq. (59) is quite constraining: we can change our fields by an *arbitrary amount, differently in each point of space-time* x , and still get the same physical results.

Now, as you know, in classical (and in quantum) electromagnetism the photon is *massless* (hence it propagates at the speed of light). If we would like to give a mass to the photon, the simplest option would be to add a *explicit mass term* of the Lagrangian of the form

$$\mathcal{L} \in \frac{1}{2} m^2 A_\mu A^\mu, \quad (61)$$

which would result in a term of the form $\sim m^2 A_\mu$ added to Maxwell's equations, that is, a non-zero mass for the photon:

$$\partial_\mu F^{\mu\nu} - \frac{1}{2} m^2 A^\nu = 0. \quad (62)$$

Why we can be confident that in electromagnetism the photon is really massless, $m = 0$, and it does not perhaps have a tiny mass consistent with all experimental constraints? Because a term of the form of Eq. (61) in the Lagrangian on the theory *does not satisfy the gauge invariance requirements*. This can be easily shown, since if I now apply a transformation of the photon field of the form Eq. (59) then the Lagrangian is not invariant. Indeed, under a gauge transformation

$$m^2 A_\mu A^\mu \rightarrow m^2 (A_\mu + \partial_\mu \eta) (A^\mu + \partial^\mu \eta) = m^2 A_\mu A^\mu + 2A_\mu \partial^\mu \eta + (\partial_\mu \eta)^2, \quad (63)$$

which is different to the original expression, and thus not gauge invariant. Therefore, a photon mass term such as Eq. (61) is not acceptable since it breaks one of the *basic symmetries of electromagnetism*, gauge symmetry (which is moreover essential to make sense of the theory at the quantum level). So Eq. (61) does not seem a good option to give a mass to the photon.

While in electromagnetism the photon is indeed massless, the Standard Model of particle physics has other forces, in particular the strong and the weak force, and in the latter case experimental evidence implies that the *bosons of the weak interaction are massive* (hence the force is short-ranges). On the other hand, we also know that the weak force can be described by a gauge symmetry, and hence one of its basic properties is that it will satisfy invariant under gauge transformations of a similar force than Eq. (59). So how it is possible to satisfy at the same time this two requirements, that is, having a theory with massive gauge bosons without breaking gauge invariance?

However, there is another way to add a mass to the photon and still satisfy the constraints from gauge symmetry. Let us introduce a *complex scalar field* ϕ which is charged under electromagnetism, in order words, it has a non-zero coupling to the photon. We also require that this scalar field exhibits *self-interactions*, that is, that it couples to itself. To maintain gauge invariance, the photon-scalar coupling must take place via the

a special type of derivative called the *covariant derivative*, in a way that the Lagrangian of the theory reads

$$\mathcal{L} = -\frac{1}{4}F_{\mu\nu}F^{\mu\nu} + (D_\mu\phi)^\dagger(D_\mu\phi) - V(\phi^\dagger\phi), \quad (64)$$

where the covariant derivative is defined as

$$D_\mu = \partial_\mu - ieA_\mu, \quad (65)$$

which takes its name because it exhibits the same properties under a gauge transformation than the field it acts upon, here the scalar field ϕ . Indeed, it is possible to check that under a $U(1)$ gauge transformation, while the photon field transforms as in Eq. (59), the scalar field transforms as

$$\phi(x) \rightarrow \exp(ie\eta(x))\phi(x), \quad (66)$$

and therefore the covariant derivative itself transforms as the field it acts upon,

$$D_\mu\phi \rightarrow \exp(ie\eta(x))D_\mu\phi, \quad (67)$$

hence the name *covariant*. You can now check that the full Lagrangian Eq. (64) is invariant under gauge transformations of the $U(1)$ type, as required. The fact that the electric charge e appears in the gauge transformation of the scalar field ϕ Eq. (66) is a consequence of the fact that this field is charged under electromagnetism (else it could not couple to the photon).

A crucial aspect of the Higgs mechanism is that in the Lagrangian Eq. (64) we have introduced a *potential* for the scalar field ϕ , which we choose to have the following shape:

$$V(\phi^\dagger\phi) \equiv -\mu\phi^\dagger\phi + \lambda(\phi^\dagger\phi)^2. \quad (68)$$

One can check that the Lagrangian Eq. (64) is invariant under the gauge transformations of electromagnetism, taking into account that the photon obeys Eq. (59) and for the scalar field we have Eq. (66). Note also that any potential for the scalar field that depends on them only through the combination $\phi^\dagger\phi$ would likewise be a consistent choice respecting gauge invariance.

In Fig. 9 we represent the Higgs potential Eq. (68) for two different possibilities for the sign of μ , either positive or negative. We see that the shape of the potential is quite different depending on the sign, in particular for $\mu > 0$ the classical minimum of the potential corresponds to a non-zero value of the scalar field ϕ . As we now show, this particular feature of the classical potential is what makes possible to *spontaneously* generate a mass for the photon. On the other hand, for $\mu \leq 0$ the minimum value of the potential (which corresponds to the *vacuum state* of the theory) is the one where the scalar field ϕ vanishes.

Classically, we know that the vacuum of the theory (that is, the state with the smallest total energy) will be the one for which the potential $V(\phi)$ has a minimum. Then, imposing this condition

$$\frac{\partial V(\phi)}{\partial\phi} = 0, \quad (69)$$

we find two possibilities for the vacuum state of our theory:

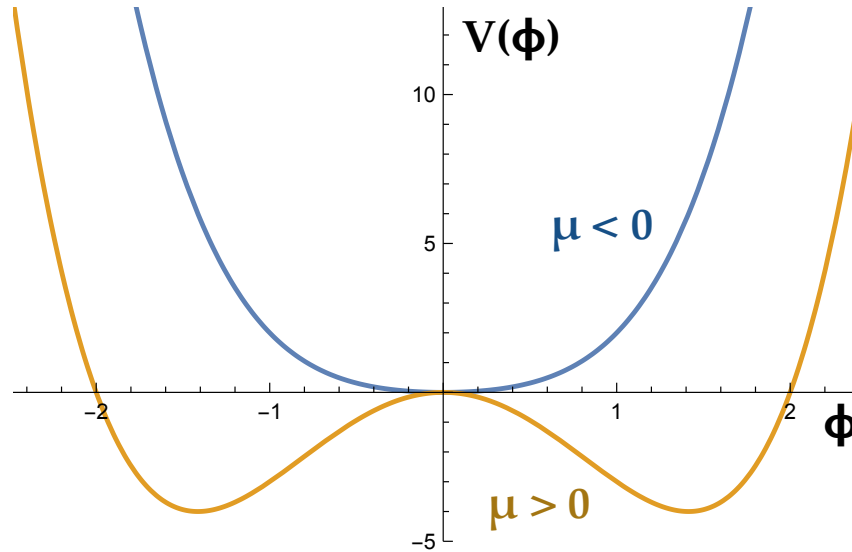


Figure 9: The Higgs potential Eq. (68) for two different possibilities for the sign of μ , either positive or negative.

- For $\mu < 0$, we find that the state of minimum energy of the theory is that where the field ϕ vanishes, $\langle \phi \rangle = 0$. In this case, the resulting theory is the standard classical electrodynamics with a massless photon coupled to a charged scalar particle.
- for $\mu > 0$ instead, the state with minimum energy is such that $\langle \phi \rangle \neq 0$, and the scalar field will acquire a vacuum expectation value (VEV) $\langle \phi \rangle = \sqrt{\mu^2/2\lambda} \equiv v/\sqrt{2}$. In this case gauge symmetry will be *spontaneously broken*, due to the fact that the vacuum (preferred configuration) is not invariant under a gauge transformation. To see these, note that either $\langle \phi \rangle = +\sqrt{\mu^2/2\lambda}$ or $\langle \phi \rangle = -\sqrt{\mu^2/2\lambda}$ are equally good solutions for Eq. (69) (as follows from the $U(1)$ rotational invariant of the theory), however only one of the two options can actually be implemented in nature, breaking thus the original gauge invariance.

Therefore, when the gauge symmetry of electromagnetism is spontaneously broken, we can parametrize the scalar field ϕ in terms of its VEV as follows

$$\phi = \frac{v+h}{\sqrt{2}} \exp\left(i\frac{Z}{v}\right), \quad (70)$$

where h would be the *Higgs boson* of spontaneously broken electromagnetism. In other words, the Higgs boson h corresponds to the excitations of the Higgs field with respect to its vacuum expectation value, and Z is called a Goldstone boson (it is required to maintain the degrees of freedom). The field Z is also real scalar fields without VEV, which can be eliminated via a field redefinition and that eventually will reappear as the longitudinal component of the (now massive) photon.

Here, it is important not to mistake the *Higgs field*, responsible for EW symmetry breaking, with the *Higgs boson*, which represents the *excitations of the Higgs field around its vacuum expectation value*. From Eq. (70) we see that $\langle h \rangle = 0$, and thus the Higgs field h now admits a particle-like interpretation (since no particles means no energy).

Using the parametrization Eq. (70) in the Lagrangian Eq. (64), in particular in the covariant derivative

that governs the interaction between the photon A_μ and the Higgs field ϕ , we find that now that the following term appears

$$\mathcal{L} \in + \frac{e^2 v^2}{2} A_\mu A^\mu, \quad (71)$$

and therefore the photon has now acquired a mass, $m_A = ev$, proportional to both its coupling e with the scalar field and to the VEV of the Higgs potential. This has been achieved respecting gauge invariance at a fundamental level, but choosing a vacuum that is instead not gauge invariant.

It is possible to check that, after spontaneously symmetry breaking, *the number of degrees of freedom* of our theory continues to be the same as before: now we have two real scalar fields, h and Z , to be compared with the starting complex field ϕ . Physically, we can say that the two degrees of freedom of the field ϕ after symmetry breaking result in the real single-particle field h and the longitudinal component of the massive photon A_μ .

In the full Standard Model, the Higgs mechanism works in a similar way but the symmetry group of electroweak theory is more complex than that of electromagnetism. In particular, after EWSB the residual symmetry of the theory is $SU(2)_L \otimes U(1)_Q$. A major difference with respect to the Abelian case is that the SM gauge group is *non-abelian*, which ultimately leads to the presence of *self-interactions between gauge bosons* (unlike in EM, where the photon does not couple to itself).

Higgs production at the LHC

In the Standard Model, once the Higgs mass is measured, then all the other properties of the Higgs boson, such as couplings and branching fractions, are uniquely determined. Thus, following the Higgs discovery in 2012, the detailed characterization of the properties of the Higgs boson is now one of the cornerstones of the LHC physics program. Indeed, most models of New Physics generically predict deviations in the Higgs couplings. Here we briefly review the various ways in which Higgs bosons can be produced and decayed at hadron colliders such as the LHC.

Higgs decays. In order to hunt for Higgs bosons, first of all we need to know what will be the final states in which the Higgs can decay. Since the Higgs couples proportional to the mass, the branching fractions will be larger to the heavier particles in the SM, provided there is enough phase space for their decays. In particular, for the decay of the Higgs to a pair of particles with mass m , kinematics requires that $m_h \geq 2m$. However, this only applies for on-shell particles: for finite-width particles, the Higgs can decay into two virtual particles or one real and one virtual so that the requirement $m_h \geq 2m$ is avoided. This explains why a 125 GeV Higgs boson can decay into ZZ or WW pairs, since one of them is off mass-shell.

At leading order, using the Feynman rules of the electroweak theory, it is possible for instance compute the decays of the Higgs boson into a fermion-anti-fermion pair:

$$\Gamma(h \rightarrow f\bar{f}) = C \frac{G_F m_f^2 m_h}{4\pi\sqrt{2}} \left(1 - \frac{4m_f^2}{m_h^2}\right)^{3/2}, \quad (72)$$

where $C = 3$ for quarks and $C = 1$ for leptons. We see that the decay width is proportional to the m_f^2 , reflecting the fact that the *Higgs couples to the mass*, and thus the Higgs interacts more strongly with more

massive particles. For this decay to be possible, one has the kinematic restriction that $2m_f < m_h$.

For the case of the decay of the Higgs boson into a pair of real Z bosons, the corresponding decay width is now given by

$$\Gamma(h \rightarrow ZZ) = \frac{G_F m_h^3 m_W^2}{16\pi\sqrt{2}m_Z^2} \left(1 - \frac{4m_z^2}{m_h^2}\right) \left(1 - \frac{4m_Z^2}{m_h^2} + \frac{12m_z^4}{m_h^4}\right). \quad (73)$$

Note that the above expression is only valid for $m_h > 2m_z$. However, decays into a ZZ pair below threshold are also possible, provided one of the Z bosons is off-shell. As mentioned above, in the SM, the decays into ZZ^* and WW^* , where the $*$ indicates that one of the weak bosons is off-shell, have relatively large branching fractions.

The preferred decay mode of Higgs bosons depends crucially on the value of m_h . On the one hand, the Higgs couples preferentially to massive particles, but it also needs enough phase space to have a large branching ratio in these specific particles. The most updated data from ATLAS and CMS provide a precise measurement of the Higgs boson mass of $m_h = 125$ GeV. In Fig. 10 we show a summary of the various decays modes of a $m_h = 125$ GeV Higgs boson, together with the corresponding branching fractions of each final state. As can be seen, the dominant channel is into a $b\bar{b}$, since the bottom quark is the heavier of the SM leptons in which the Higgs is kinematically allowed to decay. While the Higgs does not couple directly to photons, since these are massless, it can couple indirectly via a top quark loop. While this branching ratio is quite small, 0.23%, it leads to a very clean final state and thus it is extensively exploited at the LHC in Higgs studies. In general a large branching fraction does not necessarily imply that this final state exhibits the highest signal significance: one needs to know as well how large are the corresponding backgrounds.

A first estimate of the statistical significance of a given production process can be computed with S/\sqrt{B} , where S is the number of signal events and B the number of background events. Since the statistical uncertainty in the background scales as \sqrt{B} , this estimator tells how likely or unlikely is to produce signal-like events from stat fluctuations of the background.

In Fig. 10 we also show the branching fractions for each final state as a function of the Higgs boson mass, from the Higgs Cross-Section Working Group [11]. The value of the Higgs mass chosen by Nature is particularly useful since it allows to probe a variety of different final states. A heavier Higgs boson would decay almost exclusively to W and Z bosons, as well as to top quarks at the highest masses.

In the 2012 discovery, the final states exploited were limited to $\gamma\gamma$ and ZZ^* . Since then, evidence for Higgs boson production has also been found in other final states, including WW^* , $b\bar{b}$ and $\tau\tau$. The goal for the next phase of the LHC is to find evidence of decays modes with smaller branching fractions, in particular to second generation quarks and leptons such as $\mu\mu$ and $c\bar{c}$.

Higgs production. Now that we know how the Higgs boson decays, let us turn to study the different ways to produce it. While the Higgs boson couples to anything with mass, at hadron colliders only a subset of processes lead to large enough cross-sections to be of phenomenological interests. These processes are

- Gluon-gluon fusion $gg \rightarrow h$
- Vector-boson fusion $qq \rightarrow hqq$ mediated by vector bosons VV
- Associated production with vector bosons $q\bar{q} \rightarrow hV$
- Associated production with top quarks $gg \rightarrow t\bar{t}h$

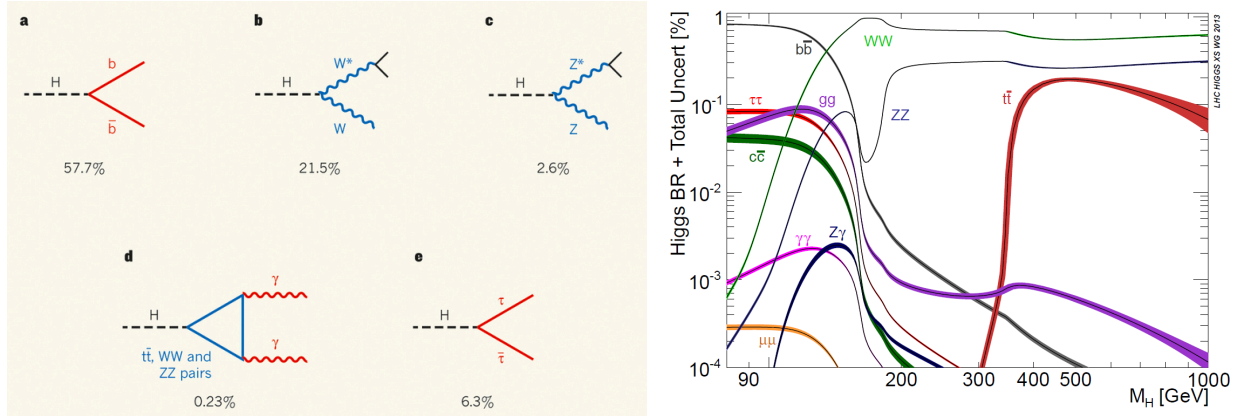


Figure 10: Left: summary of the various decays modes of a $m_h = 125$ GeV Higgs boson, together with the corresponding branching fractions of each final state. Right: the branching fractions for each final state as a function of the Higgs boson mass, from the Higgs Cross-Section Working Group.

In Fig. 11 we show the Feynman diagrams corresponding to these different production processes.

For a SM Higgs boson of $m_h = 125$ GeV, the production process with a higher cross-section is the gluon-fusion process, which proceeds via a top quark loop. The calculation is simplified in the limit in which the top quark mass is much larger than the higgs mass, $m_t \gg m_h$, since then the top quark loop reduces to a point-like vertex. In this limit it can be checked that the squared matrix element reads

$$|\mathcal{M}(gg \rightarrow h)|^2 = \frac{\alpha_s^2(m_h) G_F m_h^4}{288\sqrt{2}\pi^2}, \quad (74)$$

and to get the partonic cross-section we need to multiply by the phase space term, which for a $2 \rightarrow 1$ process is a trivial delta function, as was the case for electroweak gauge boson production,

$$\tilde{\sigma}(gg \rightarrow h) = \frac{\pi}{\sqrt{s}} \delta(\hat{s} - m_h^2) |\mathcal{M}(gg \rightarrow h)|^2, \quad (75)$$

and upon convolution with the gluon PDFs, the hadronic cross-section is obtained.

Another important production process is associated production the Higgs boson with electroweak gauge bosons. While the production cross-sections are smaller than for the gluon-fusion channel, the usefulness of Wh and Zh production is that the additional weak gauge boson can be cleanly reconstructed, providing a useful handle to discriminate between signal and background. In this case the partonic cross-sections, for example in the case of Zh production, are given as follows

$$\hat{\sigma}(q\bar{q} \rightarrow zh) = \frac{(G_F m_Z^2)^2}{9\pi} (V_q^2 + A_q^2) \frac{p_Z}{\sqrt{s}} \frac{3m_z^2 + p_Z^2}{(\hat{s} - m_Z^2)^2}, \quad (76)$$

where we have defined

$$p_Z^2 = \frac{1}{4\hat{s}} (\hat{s}^2 + M_Z^4 + m_h^4 - 2\hat{s}m_Z^2 - 2\hat{s}m_h^2 - 2m_V^2 m_h^2). \quad (77)$$

which is enhanced for partonic center-of-mass energies similar to the weak boson mass since this is a s -channel process with the weak boson in the propagator.

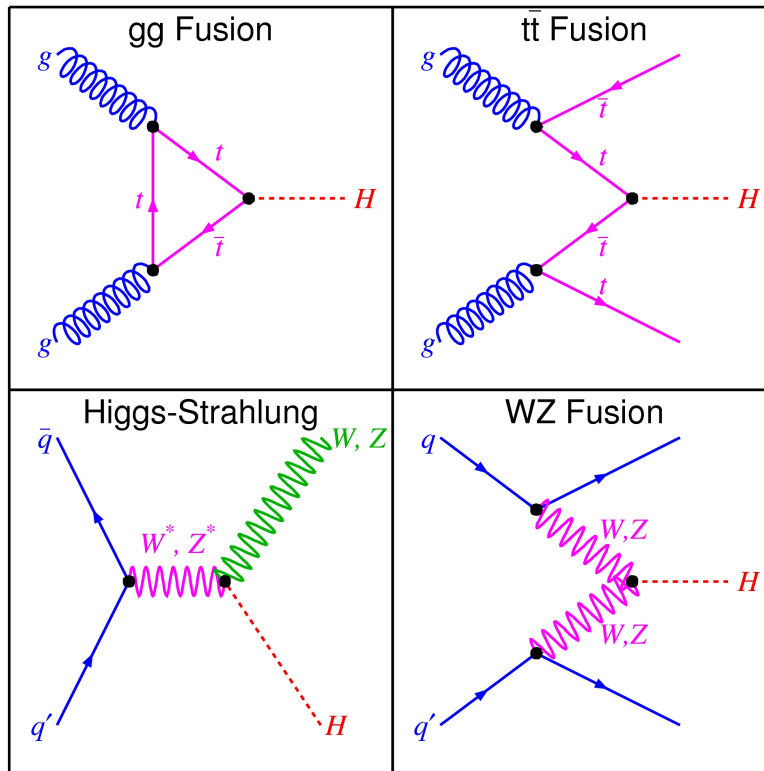


Figure 11: The four main production channels for the production of Higgs boson at the large hadron collider.

In Fig. 12 we show the cross-section for Higgs production at hadron colliders for $m_h = 125$ GeV, for different production channels and collider center-of-mass energies. We also show the cross-section for Higgs production at the LHC 8 TeV for different production channels, as a function of m_h .

There are a number of interesting points to remark from Fig. 12:

- The gluon-fusion process is dominant for any Higgs mass, except for $m_h \simeq 1$ TeV where the VBF process becomes of the same order.
- The production rate of a Higgs boson in association with top quarks is small at the LHC, but becomes greatly enhanced at a future higher energy collider due to the increased center of mass energy.
- Higgs pair production is smaller than single Higgs production by several orders of magnitude.

Given that each of the production processes listed in Fig. 11 has a complementary sensitivity to the Higgs properties, it is crucial to measure (and predict theoretically) them with the highest possible accuracy. For instance, one of the goals of Run II of the LHC is to find evidence of Higgs production in association with a top-antitop quark pair, which provides direct sensitivity to the Yukawa coupling between the top quark and the Higgs (which is the largest to all Higgs couplings to matter particles).

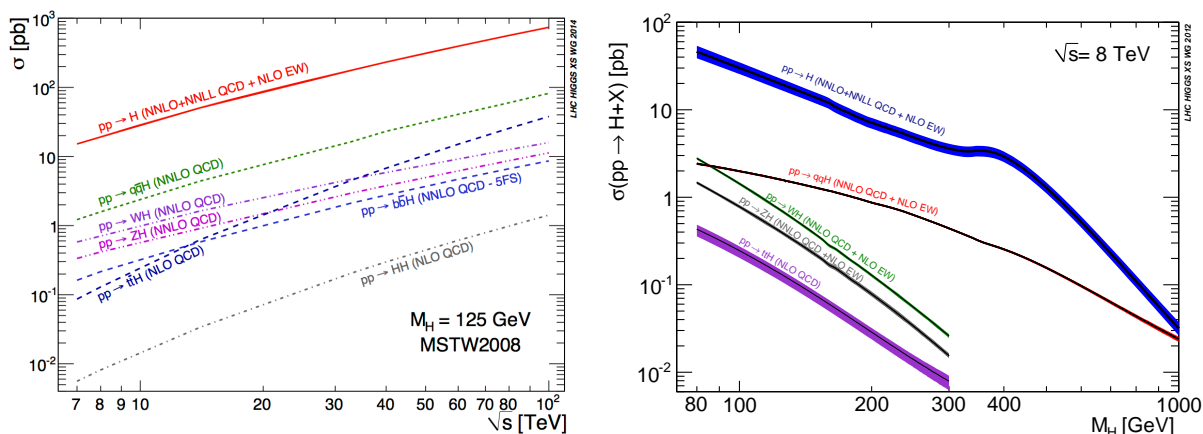


Figure 12: Left plot: the cross-section for Higgs production at hadron colliders for $m_h = 125$ GeV, for different production channels and collider center-of-mass energies. Right plot: the cross-section for Higgs production at the LHC 8 TeV for different production channels, as a function of m_h .

Jet reconstruction and substructure

A very important topic for LHC analysis is that of the *reconstruction* and *substructure analysis* of hadronic jets. Naively, jets can be thought of *collimated bunches of hadrons* arising in high energy collisions, and that can be traced back to the production of energetic quarks or gluons in the hard scattering. However, jets are fundamentally ambiguous concept. Formally, a jet definition needs to be introduced, that is, a systematic procedure that projects away multi-particle dynamics, trying to get as close as possible to a single hard quark or gluon. As shown in Fig. 13, there is no unique jet definition, and starting from the same set of final-state particles we can end up with a different jet collection.¹ Moreover, a sensible jet definition should be applied in the same algorithmic way to partons, hadrons and calorimeter cells.

Another crucial property of a jet definition is that it should be *infrared and collinear safe*, that is, provide sensible results to all orders in the QCD perturbative expansion. In particular, this implies that a jet cross-section, computed in pQCD with a given jet algorithm, should be unchanged if any of the particles undergoes a *soft* or a *collinear splitting*, that is, if one final-state particle (say a quark or a gluon) splits into two particles which are very close to each other, or if one particle radiates a very soft (small energy) secondary particle. An example of a IRC unsafe definition would be the following:

¹plots from Gavin Salam, <https://gsalam.web.cern.ch/gsalam/talks/>.

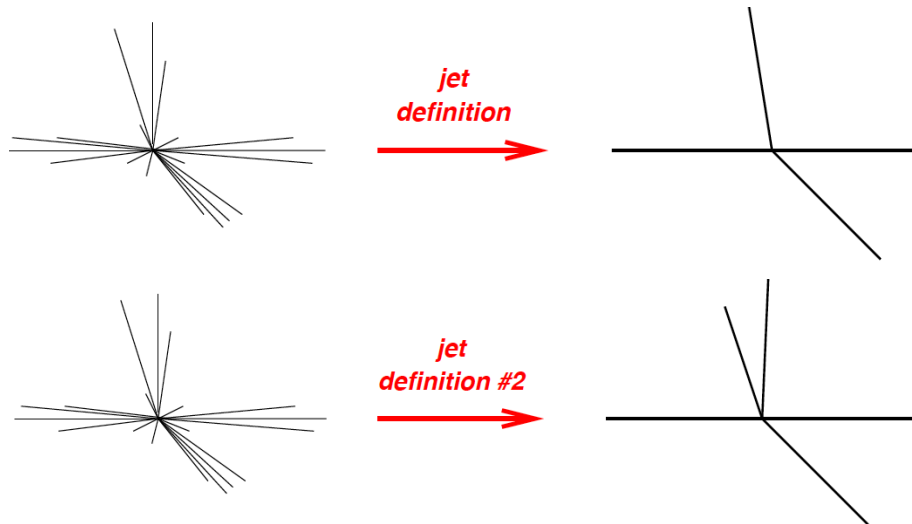


Figure 13: A jet definition is a systematic procedure that projects away multi-particle dynamics, trying to get as close as possible to a single hard quark or gluon.

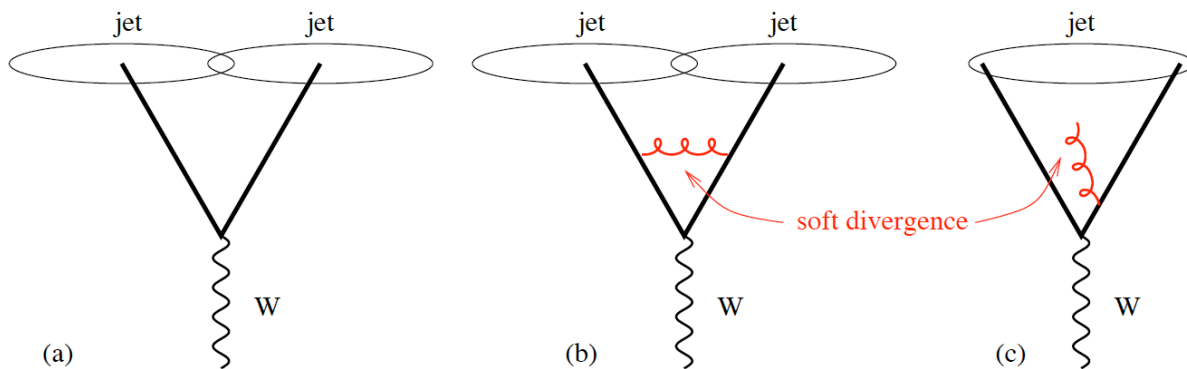


Figure 14: An example of an IRC unsafe jet definition, applied to the hadronic decays of a W boson. The emission of a collinear gluon changes the final jet collection, which this is not the case of course for the virtual correction. This means that real and virtual divergences will not cancel out and the resulting jet cross-section will be infinite.

since we see the emission of an arbitrarily soft parton merges the two jets that would otherwise be separated, spoiling the cancellation of real and virtual soft divergences and producing an infinite result. With this motivation, all the jet reconstruction algorithms used for the analysis of LHC data are now IRC safe.

The most popular jet reconstruction algorithm at the LHC is known as the *anti- k_T algorithm*. The basic idea of this algorithm is to cluster pairs of partons sequentially following some measure of their *distance*. The algorithm works as follows:

- (a) Make a list of all final-state particles in your collision (can be partons, hadrons, calorimeter cells, etc - the definition is purely algorithmic!)
- (b) Now compute a *distance* between a pair of particles, each with transverse momentum $p_{T,i}$, rapidity y_i

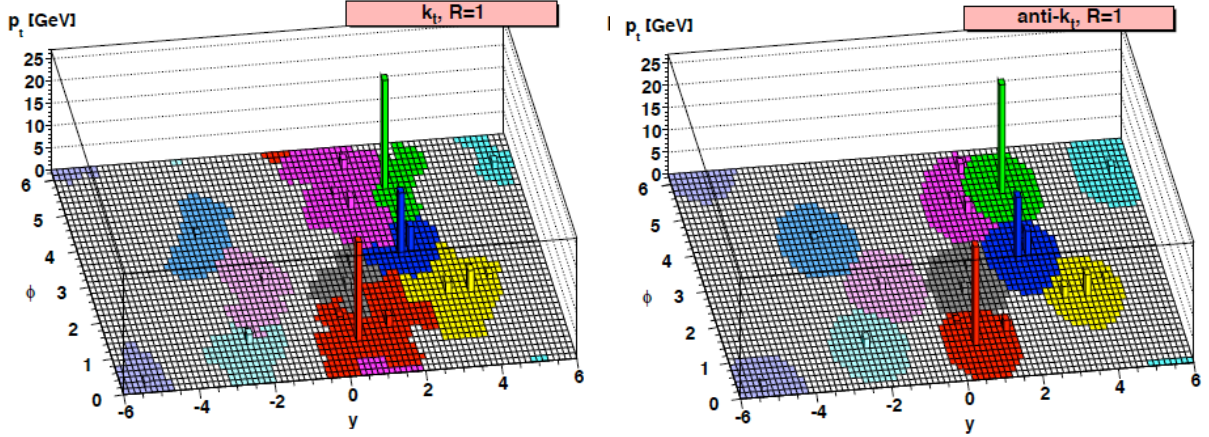


Figure 15: The catchment area of two jet algorithms, with $R = 1$: the k_T algorithm and the anti- k_T algorithm. It is clear that the second produces much more regular jets than the first of the algorithms, and thus is advantageous *i.e.* to reduce the background noise (UE, MPI, PU) that affects hadronic collisions.

and azimuthal angle ϕ_i :

$$d_{ij} = \min \left(p_{T,i}^{-2}, p_{T,j}^{-2} \right) \frac{(y_i - y_j)^2 + (\phi_i - \phi_j)^2}{R^2}. \quad (78)$$

where R is the jet radius, the fundamental parameter of the algorithm, which is a measure of how large the jet is (in the (η, ϕ) plane). We also compute the distance of particle i with the proton beam

$$d_{iB} = p_{T,i}^2. \quad (79)$$

- (c) Find the minimum distance. If it is a d_{ij} , recombine the two particles by adding their four-momentum. Else, *declare particle i to be a jet* and remove it from the list of particles.
- (d) Continue the algorithm until the list of particles is empty and thus all particles have been assigned to jets.

An important property of the anti- k_T algorithm is that its *catchment area* [13] (the area in which each picks up soft particles) is relatively regular, and this is a very beneficial property for jet energy calibration as well as for the subtraction of underlying event and pileup. In Fig. 15 we show the catchment area of two jet algorithms, with $R = 1$: the k_T algorithm and the anti- k_T algorithm, which is very similar with only difference that in this case the distance is defined as

$$d_{ij} = \min \left(p_{T,i}^{-2}, p_{T,j}^{-2} \right) \frac{(y_i - y_j)^2 + (\phi_i - \phi_j)^2}{R^2}. \quad (80)$$

It is clear that the second produces much more regular jets than the first of the algorithms.

This property of the anti- k_T algorithm allows an easier removal of hadronic noise, which is typically proportional to the jet area. Indeed, in hadronic collisions such as those of the LHC, we have additional activity than just the hard primary quark-gluon scattering. LHC collisions will typically also exhibit

- *Underlying Event* (UE): additional hadronic activity from the same proton-proton collision
- *Multiple Parton Interactions* (MPI) and double parton scattering (DPS): additional hard hadronic collisions from the same proton-proton collision as the primary scattering.
- *Pile-Up* (PU): additional hard and soft collisions from other proton-proton collisions in the same bunch crossing.

Techniques to allow to reduce the contamination from all these effects are crucial to perform clean measurements at the LHC. And in this respect the regular jet area provided by the anti- k_T algorithm is certainly advantageous. At Run II of the LHC, and even more at the future High-Luminosity upgrade, PU in particular will be a major issue, with up to 200 interactions per bunch crossing, so much that it requires replacing parts of the LHC detectors to deal with this significant increase of hadronic activity.

Jet substructure

Concerning the analysis of hadronic jets at the LHC, a topic that has received a lot of attention recently is that of their *internal substructure*. The motivation to look closer to the internal structure of jets is provided by the following observation. Consider the decays of a heavy resonance with a mass at the electroweak scale, say $m \gtrsim v$. Typically, due to the limited phase space, it will be produced with a small boost, and thus, if decays to QCD partons, the resulting jets will be well separated. However, at the LHC a new kinematical regime becomes available: that where the EW-scale resonance is produced with a *very large boost*, $p_T \gg m$: the kinematics of the resulting final state will be very different from those of the rest frame decay. In these conditions, the subsequent hadronic decays of the resonance end up being collimated into a single jet, becoming thus indistinguishable from the overwhelming QCD background - unless jet substructure tools are used.

The situation is illustrated in Fig. 16. A heavy resonance, such as a W boson or a top quark, produced with a large enough boost, $p_T \gg m$, when decaying hadronically, the final state becomes indistinguishable from that of QCD jets. This seems a major problem, since it seems one would be missing many events of important electroweak processes because of the dominance of the QCD jet backgrounds. Given that many BSM scenarios involve the production of boosted heavy resonances, a major limitation to the LHC program might be feared. Fortunately, we can use our understanding of QCD radiation to distinguish background from interesting signals even in the boosted regime. For instance, to reconstruct a top quark which decays hadronically, $t \rightarrow bq\bar{q}'$, the traditional signature is of three resolved jets with invariant mass m_{bqq} similar to that of the top quark. But what happens if all the decay products of a top quark are collimated within a single jet? Here jet substructures provide a unique handle to separate signal from background events.

To quantify which is the kinematic regime relevant for jet substructure, let us consider one of the most paradigmatic examples, namely the decay of a *boosted Higgs boson* into a $b\bar{b}$ pair [12]. The processes is illustrated schematically in Fig. 17. For simplicity, we assume that the Higgs has been produced centrally, and take the azimuthal angle to be $\phi = 0$.

Using the four-momenta parametrisation for hadronic collisions that was introduced above, we can write the four-momentum of the Higgs boson as follows:

$$p_H = \left(\sqrt{m_H^2 + p_{T,H}^2}, p_{T,H}, 0, 0 \right), \quad (81)$$

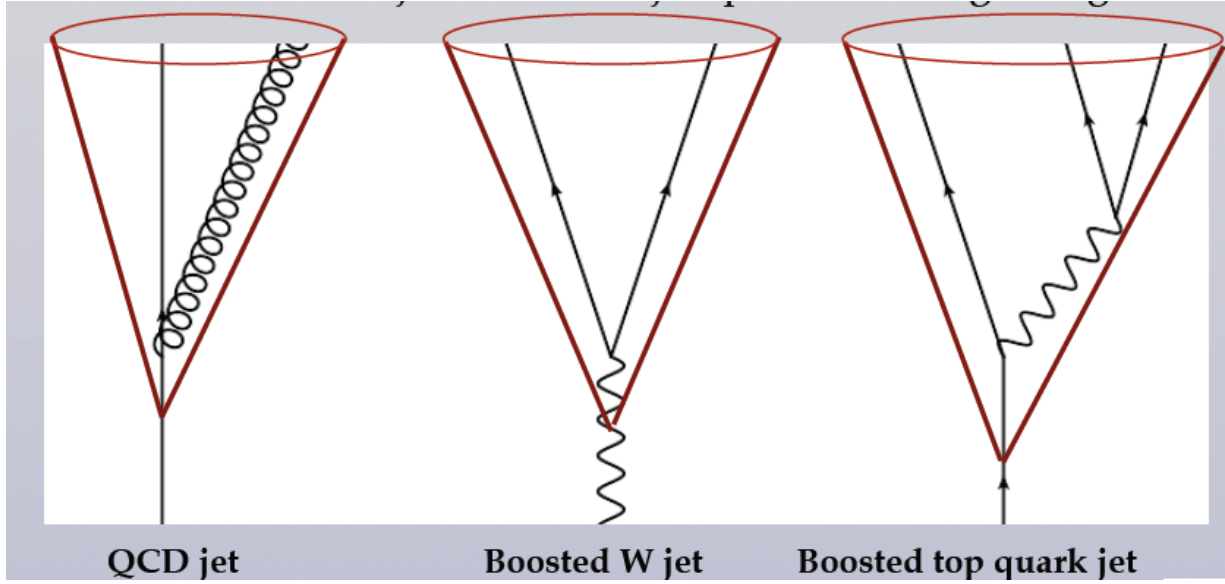


Figure 16: If a heavy resonance is produced with a large enough *boost*, meaning that their transverse momentum is much larger than their mass $p_T \gg m$, then when decaying hadronically the final state becomes indistinguishable from that of QCD jets - unless one looks inside at the jet substructure.

and that of the decay bottom quarks

$$p_b = \left(z \sqrt{m_H^2 + p_{T,H}^2}, p_{x,b}, 0, p_{z,b} \right), \quad (82)$$

$$p_{\bar{b}} = \left((1-z) \sqrt{m_H^2 + p_{T,H}^2}, p_{x,\bar{b}}, 0, -p_{z,b} \right), \quad (83)$$

where z is the fraction of the Higgs boson original energy that is being carried by the b quark, and correspondingly $(1-z)$ is the energy fraction being carried by the \bar{b} quark.

Now using four-momentum conservation and neglecting the small masses of the bottom quarks, we find that the kinematics of the process is uniquely defined in terms of three variables:

- The Higgs boson mass, m_H ,
- The Higgs transverse momentum, $p_{T,H}$,
- and the fraction of energy carried by the bottom quark z (which determines the asymmetry of the decay).

Now doing some algebra, imposing four-momentum conservation, and neglecting the masses of the bottom quarks, it is possible to show that

$$p_{x,b} = \frac{p_{T,H}}{2} + (2z-1) \frac{p_{T,H}^2 + m_H^2}{2p_{T,H}}, \quad (84)$$

$$p_{x,\bar{b}} = \frac{p_{T,H}}{2} - (2z-1) \frac{p_{T,H}^2 + m_H^2}{2p_{T,H}}, \quad (85)$$

$$p_{z,b} = \left[(p_{T,H}^2 + m_H^2) \left(z^2 - z + \frac{1}{2} \right) - \frac{p_{T,H}^2}{4} - (2z-1)^2 \frac{(p_{T,H}^2 + m_H^2)^2}{4p_{T,H}^2} \right]^{1/2}. \quad (86)$$

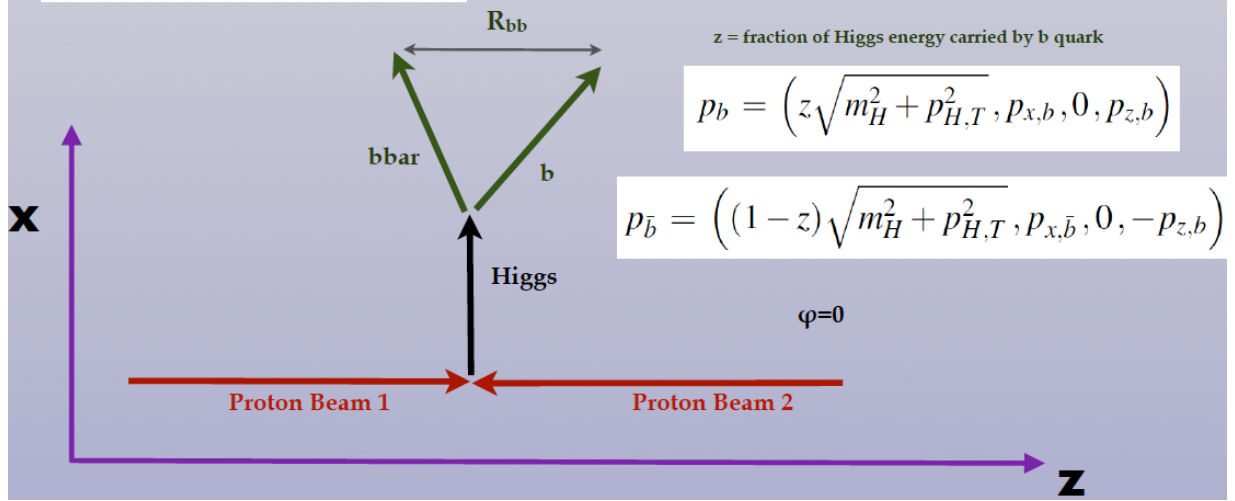


Figure 17: Scheme for the central production of a Higgs boson in a hadronic collision, followed by the decay into a pair of bottom and anti-bottom quarks.

The above formulae are valid in all generality. Now let us consider the *boosted regime*, defined as follows: an hadronic system is considered boosted when its transverse momentum is much larger than its invariant mass, and in this case this condition leads to $p_{T,H} \gg m_H$. Under this assumption, we find a substantial simplification to end up with

$$p_{x,b} = z p_{T,H}, \quad (87)$$

$$p_{x,\bar{b}} = (1-z) p_{T,H}, \quad (88)$$

$$p_{z,b} = \sqrt{z(1-z)} m_H. \quad (89)$$

Therefore, in the boosted regime, the angular separation between the bottom and anti-bottom quarks, $R_{b\bar{b}}$, will be given by

$$R_{b\bar{b}} = \frac{p_{z,b}}{p_{x,b}} - \frac{p_{z,\bar{b}}}{p_{x,\bar{b}}} = \frac{1}{\sqrt{z(1-z)}} \frac{m_H}{p_{T,H}}. \quad (90)$$

Eq. (90) allows to determine when the boosted regime kicks in at the level of final state topology. If we have a jet definition with jet radius R , then, if the transverse momentum of the Higgs boson is such that $R \geq R_{b\bar{b}}$, the two b quarks will end up collimated into a single jet, and there traditional Higgs reconstruction, based on two separate b -tagged jets, becomes impossible. For $R = 0.5$ and $z = 1/2$, we find that in the case of $H \rightarrow b\bar{b}$ the boosted regime is relevant when $p_{T,H} \geq 500$ GeV.

This analysis indicates that for the case of Higgs production at high p_T followed by the decay into a $b\bar{b}$ pair, for $p_{T,H} \geq 500$ GeV we will suffer a significant reduction of the signal reconstruction efficiency unless jet substructure techniques are used.

References

- [1] M. E. Peskin and D. V. Schroeder, “An introduction to quantum field theory,” Reading, USA: Addison-Wesley (1995).
- [2] M. D. Schwartz, “Quantum Field Theory and the Standard Model,” Cambridge University Press (2014).
- [3] J. Collins, “Foundations of perturbative QCD,” Cambridge monographs on particle physics, nuclear physics and cosmology (2014).
- [4] C. P. Burgess and G. D. Moore, “The standard model: A primer,” Cambridge, UK: Cambridge Univ. Press (2007).
- [5] R. K. Ellis, W. J. Stirling and B. R. Webber, “QCD and collider physics,” Camb. Monogr. Part. Phys. Nucl. Phys. Cosmol. **8**, 1 (1996).
- [6] G. Dissertori, I. G. Knowles and M. Schmelling, “Quantum Chromodynamics: High energy experiments and theory,” International series of monographs on physics, 115, Oxford Science Publications.
- [7] J. Rojo, “The Strong Interactions and LHC phenomenology”, lecture notes available online at <http://juanrojo.com/teaching>
- [8] G. Zanderighi, “QCD and collider physics”, lecture notes available online at <http://www2.physics.ox.ac.uk/sites/default/files/QCDLectures.pdf>
- [9] P. Nason, “Introduction to QCD”, lecture notes available online at <http://moby.mib.infn.it/~nason/misc/QCD-intro.ps.gz>
- [10] M. Beneke, A. Maier, J. Piclum and T. Rauh, Nucl. Phys. B **899**, 180 (2015) doi:10.1016/j.nuclphysb.2015.07.034 [arXiv:1506.06865 [hep-ph]].
- [11] D. de Florian *et al.* [LHC Higgs Cross Section Working Group], arXiv:1610.07922 [hep-ph].
- [12] J. M. Butterworth, A. R. Davison, M. Rubin and G. P. Salam, Phys. Rev. Lett. **100**, 242001 (2008) doi:10.1103/PhysRevLett.100.242001 [arXiv:0802.2470 [hep-ph]].
- [13] M. Cacciari, G. P. Salam and G. Soyez, JHEP **0804**, 005 (2008) doi:10.1088/1126-6708/2008/04/005 [arXiv:0802.1188 [hep-ph]].